ACS Partner Journal

CHEMICAL & BIOMEDICAL IMAGING

pubs.acs.org/ChemBioImaging

Article

Label-Free, Noninvasive Bone Cell Classification by Hyperspectral Confocal Raman Microscopy

Zachary T. Piontkowski,* Dulce C. Hayes, Anthony McDonald, Kalista Pattison, Kimberly S. Butler, and Jerilyn A. Timlin*

Cite This: *Chem. Biomed. Imaging* 2024, 2, 147−155

Read Online

ACCESS | Metrics & More | Article Recommendations | Supporting Information

ABSTRACT: Characterizing and identifying cells in multicellular *in vitro* models remain a substantial challenge. Here, we utilize hyperspectral confocal Raman microscopy and principal component analysis coupled with linear discriminant analysis to form a label-free, noninvasive approach for classifying bone cells and osteosarcoma cells. Through the development of a library of hyperspectral Raman images of the K7M2-wt osteosarcoma cell lines, 7F2 osteoblast cell lines, RAW 264.7 macrophage cell line, and osteoclasts induced from RAW 264.7 macrophages, we built a linear discriminant model capable of correctly identifying each of these cell types. The model was cross-validated using a k-fold cross validation scheme. The results show a minimum of 72% accuracy in predicting cell type. We also utilize the model to reconstruct the spectra of K7M2 and 7F2 to determine whether osteosarcoma cancer cells and normal osteoblasts have any prominent differences that can be captured by Raman. We find that the main differences between these two cell types are the prominence of the β-sheet protein secondary structure in K7M2 versus the α-helix protein secondary structure in 7F2. Additionally, differences in the CH_2 deformation Raman feature highlight that the membrane lipid structure is different between these cells, which may affect the overall signaling and functional contrasts. Overall, we show that hyperspectral confocal Raman microscopy can serve as an effective tool for label-free, nondestructive cellular classification and that the spectral reconstructions can be used to gain deeper insight into the differences that drive different functional outcomes of different cells.

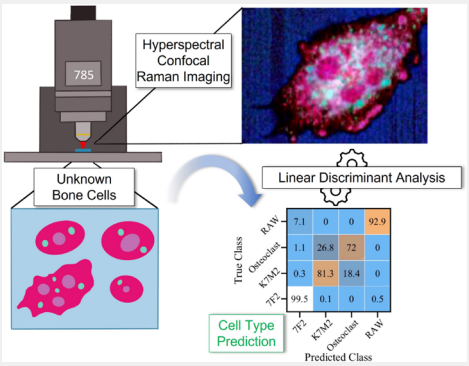

KEYWORDS: *Spectral Imaging, Raman, Osteoblast, Osteoclast, PCA, LDA, Bone*

INTRODUCTION

Multicellular *in vitro* model systems are growing in both complexity and popularity as tools to better understand the complex nature of disease. The ability to identify the cell type of individual living cells within these multicellular systems in real time has the potential to provide key information about cell-to-cell interactions necessary to understand disease states. Optical microscopy methods are attractive for this task because they are nondestructive, provide spatial resolution, and are amenable to *in vitro* and *in vivo* applications. However, cells themselves absorb little light, can have similar morphological features, and can be tightly intertwined in tissue and tissue models, making native cells hard to visualize and distinguish from other cell types without enhancement. The most widespread solution to this problem is the use of fluorescent dyes and labels. While these tools can provide detailed structural and molecular information, these labels often involve procedures such as fixation and cell permeabilization that are incompatible with living cells. Even with labels compatible with living cells, issues can arise in the cellular response to the label, including concentration dependent phototoxicity, perturbations in cellular or protein function, and limitations in labeling duration.[1] Methods such as expression of green fluorescent protein (GFP), which allows visualization of cells without an exogenous fluorophore, require modification of the cell to express the fluorescent protein, which can also alter cell behavior. Additionally, the need to label multiple cell types can be time-consuming. In contrast, label-free imaging utilizes native signatures within cells and tissues. A wide range of label-free techniques have been developed including photoacoustic,[2] fluorescence lifetime,[3] surface enhanced Raman spectroscopy (SERS),[4] and Raman microscopy.[5] Hyperspectral confocal Raman microscopy is gaining popularity as an analytical tool for biological and biomedical specimens as the Raman spectra of cells and tissues provides a detailed molecular fingerprint containing both qualitative and quantitative biochemical information overlaid with morphological information.[6] Due to the comprehensive information available, hyperspectral confocal Raman microscopy is being evaluated for use in

Received: October 16, 2023
Revised: December 6, 2023
Accepted: December 30, 2023
Published: January 24, 2024

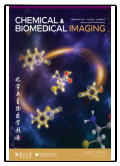

diagnostics of biological fluids and histology specimens as well as drug pharmacokinetics and cell-based therapies.[6] It should be noted that Raman spectroscopy has also been used extensively to assess the chemical composition of bone.[7−10] However, our focus in this work is on cell lines of bone. Hyperspectral confocal Raman microscopy has been demonstrated to differentiate between normal and tumor cells, different cell stages, and different cell types.[4,11−13] One advantage of hyperspectral confocal Raman spectroscopy over, e.g., SERS, for the identification of normal versus tumor bone cells[4,13] is that hyperspectral imaging provides a Raman signal across the entirety of the cell. Different features of the cell, e.g., nuclei versus lipid membrane, will elicit different Raman responses. These varied responses can be exploited to determine the basis for differentiation of the cell type. For example, if cells can be classified as different, is it because the responses from their nuclei are different? Or does it occur because the lipid membrane response is different? This information provides key insights into the biochemical markers that permit differentiation within a multicellular model. The ability to differentiate between similar cells without the use of exogenous fluorescent or other labels or substrates has implications in diagnostics but also presents unique opportunities for monitoring cellular interactions in multicellular model systems and facilitates studies of cancer cell interactions with normal cells in their environment, such as multicell models of bone cancer.

The cellular components of bone are highly dynamic and can change to facilitate bone homeostasis, growth, and remodeling.[14,15] Within the bone, the mature osteoclasts and osteoblasts signal to each other as well as to potential precursor cells to initiate the development of new osteoclasts or osteoblasts, as well as bone growth and remodeling. This signaling encompasses both released soluble factors as well as membrane bound factors,[15] making the ability to differentiate cells in complex multicellular model systems important for mechanistic and therapeutic studies. This multicellular system becomes even more complex when osteosarcoma tumor cells are present. Osteosarcoma is the most common bone cancer and can be either osteoblastic or osteolytic in behavior, which is mitigated through signaling to osteoclasts and osteoblasts.[16] Due to the low native contrast of mammalian cells, including osteosarcoma, osteoblasts, and osteoclasts, multicellular models often rely on staining of fixed and permeabilized systems with cells differentiated by morphological features or binding of specific antibodies.[17−19] While morphological features, such as the number of nuclei and cell shape, can readily differentiate osteoclasts, osteoblasts, and osteoclast precursor cells using nuclear and actin staining, this task becomes more difficult if the model system also incorporates any cell types that are morphologically similar. Here, hyperspectral confocal Raman microscopy may be able to provide a distinct advantage as it has previously demonstrated the ability to differentiate normal from cancerous cells in both primary cells and cell lines.[11] Hyperspectral confocal Raman microscopy has previously been limitedly applied to bone cells and has shown the capacity to follow osteoblast differentiation and osteosarcoma response to therapeutics in living cells in real time.[20,21] To extend these previous studies, we employ hyperspectral confocal Raman microscopy to identify common mouse bone and osteosarcoma model cells based on their unique spectral signatures. In this work, the K7M2 osteosarcoma cell line was selected as it is a common syngeneic mouse model of osteolytic osteosarcoma capable of forming lytic tumors in the tibia and jaw, as well as having a high metastatic potential.[22−24] Mouse macrophages (RAW 264.7), osteoclasts differentiated from the mouse macrophages, and the mouse osteoblast cell line 7F2 were selected, as they form a likely set of cells for an osteosarcoma model.

In the following, we present hyperspectral confocal Raman imaging of each of the aforementioned cell lines. We show that the characteristic features of each of these cell line spectra can be captured by a principal component analysis (PCA) dimensionality reduction. The characteristic principal components (PCs) are then used to train a linear discriminant analysis (LDA) model, which through cross-validation, is shown to accurately classify each of the cell types. Through reconstruction of the spectra from the PCA-LDA model, we are able to extract the characteristic features of each cell line, which lends them to accurate classification. These characteristics are analyzed in detail for the K7M2 osteosarcoma cell line and the 7F2 osteoblast cell line, which extracts the biochemical markers that distinguish the cancerous osteosarcoma from the normal osteoblast. Finally, implications for diagnostic, *in vitro*, and *in vivo* application of this label-free classification technique are discussed.

METHODS

Cell Culture

Mouse macrophage cell line RAW 264.7, osteosarcoma cell line K7M2-wt, and osteoblast cell line 7F2 were purchased from ATCC. RAW 264.7 and K7M2-wt were maintained in Dulbecco's Modified Eagle's Medium (DMEM, GIBCO) supplemented with 10% (v/v) fetal bovine serum (FBS, Hyclone) and 100 units/mL Penicillin and 100 μg/mL Streptomycin (Pen-Strep, Gibco). 7F2 cells were maintained in alpha minimal essential media (alpha MEM, GIBCO) containing 2 mM L-glutamine and 1 mM sodium pyruvate and without ribonucleosides and deoxyribonucleosides. The alpha MEM media was supplemented with 10% (v/v) FBS and 100 units/mL Penicillin and 100 μg/mL Streptomycin. Cells were cultured at 37 C and 5% CO_2.

To prepare the RAW 264.7, K7M2-wt, and 7F2 cells for imaging, ethanol sterilized fused quartz coverslips (Technical Glass Products) were placed in a 100 mm dish. To the 100 mm dish were added the cells of interest, and they were allowed to adhere overnight. Imaging was performed in a HEPES-based imaging medium. Imaging medium was prepared at 2.5× and contained 375 mM NaCl, 50 mM HEPES, 2.5 mM $CaCl_2$, 12.5 mM KCl, and 2.5 mM $MgCl_2$, pH 7.4.[25] On the day of use, imaging medium was diluted to 1× and 95 mg of glucose and 95 mg of bovine serum albumin were added per 50 mL of imaging medium. To mount the quartz coverslips, an *in situ* incubation chamber (Frame-Seal, Bio-Rad) was adhered to a quartz slide and filled with the freshly prepared imaging medium. The quartz coverslips with adhered cells were then gently rinsed in imaging buffer and inverted onto the filled incubation chamber. Prepared slides were imaged immediately. Osteoclasts were induced from RAW 264.7 cells based on published methods and described briefly here.[26] To create osteoclasts for imaging, ethanol sterilized quartz coverslips were placed in a 100 mm dish. To the quartz coverslip in a 100 mm dish, RAW 264.7 cells below passage 8 were plated at 5.0×10^4 cells per quartz coverslip in DMEM + 10% FBS and allowed to adhere overnight (day 0). The following day (day 1), the media was replaced with DMEM + 10% FBS supplemented with 25 ng/mL recombinant mouse RANKL (R&D systems). Media was replaced again with RANKL supplemented media on days 3 and 5. Induced osteoclasts were imaged on days 6 and 7 by mounting in imaging media following the same method described above.

https://doi.org/10.1021/cbmi.3c00106
Chem. Biomed. Imaging 2024, 2, 147−155

Hyperspectral Confocal Raman Microscopy

Raman images were collected by using a WITec Alpha 300R confocal Raman microscope. A 785 nm laser was used as the excitation source. The laser was fiber-coupled through a single-mode fiber to a holographic beam splitter that directed the beam to the entrance pupil of an objective. A 50×, 0.55 NA objective (Zeiss) was used for all measurements. The back plane of the coverslip, onto which the cells were adhered, was chosen as the focal plane for imaging. Scattered light was collected back through the objective in a backscattering geometry and directed to a 50 μm diameter, multimode fiber. The collection fiber was coupled to a single grating spectrometer equipped with a 600 g/mm grating blazed at 750 nm. The grating position was chosen to provide a Raman spectral window ranging from 134 to 1912 cm^{-1}. The spectral resolution under these conditions was between ≈1.5 and ≈1.8 cm^{-1}/pixel. Images were collected with a 0.5 μm step size using an integration time between 0.5 and 2 s per step. Maps of each cell type were collected and added to the total data set for analysis. The data set comprised maps of K7M2 (62400 pixels), 7F2 (20664 pixels), RAW (68100 pixels), and osteoclast (26808 pixels). The pixel counts represent the total number of pixels spanning the imaged area for each respective cell type over multiple images. For our chosen window of spectral analysis, there are 511 spectral channels for each spatial pixel, resulting in a hyperspectral volume of up to ≈35 million pixels per cell. The number of images collected was chosen to balance the total number of pixels representing each cell, thus ensuring the net analyte signal for each of the cell lines was similar.

Spectral Processing and PCA-LDA Analysis

Postprocessing of the data included cosmic ray removal, median filter spectral smoothing, and background subtraction. Each of these was performed using WITec Project FIVE, version 5.2 software. Cosmic ray removal was performed using the built-in algorithm with a filter size of 4 and a dynamic factor of 4. Median filter smoothing was performed with a filter size of 1. Background subtraction was performed using a rounded shape background with a "shape size" of 150. Here, the background is subtracted using a rounded shape, which is approached to the spectrum from below, pixel-by-pixel. The "shape size" of 150 is large and enforces the use of a large rounded shape, which preserves sharp spectral features but removes background fluorescence and broad quartz signal. After processing, spectra were trimmed to the range of 900 to 1740 cm^{-1}. Spectra were then normalized and the mean centered. Raman maps of all cells were flattened and combined into a single matrix with the Raman shift axis along the rows and pixel along the columns. For simplicity, and to more closely approximate what would be expected in multicellular *in vitro* model systems where intracellular space would contain excreted compounds, we have included both the cell and the cell surroundings in the data set. Improvements to the model may be made by segmenting the cell from its surroundings so that the surrounding pixels are not artificially classified as cell types. We find, however, that the trade-off for simplicity results in sufficient accuracy for the scope of this work.

Principal component analysis (PCA) was performed using the *pca* function in Matlab. PCA was used to extract the principal component (PC) coefficients or loadings as well as the PC scores. The PC score matrix was used to build a linear discriminant (LD) model according to the known cell assignment for each pixel. PC1, PC2, PC4, and PC5 were used to build this model, as PC3 was found to represent the HEPES-based imaging medium spectrum, with a sharp peak at ≈1040 cm^{-1},[27] which could not be consistently removed prior to PCA by other means. PC1−5 accounted for 74% of the total variance and produced good reconstructions of the spectra. Higher PCs were found to add noise back into the reconstructions. Linear discriminant analysis (LDA) was performed by treating the output PC scores as input predictors for the model. Class labels are given by the known cell assignment for each pixel index in the score matrix. LDA was performed using the Matlab function *fitdiscr* with a pseudolinear discriminant type, where all classes are assumed to have the same covariance matrix and the covariance matrix is inverted using the pseudo inverse. To obtain scores projected onto the LD eigenvectors, the eigenvalue problem is solved for the within-class covariance, σ_w, and between-class covariance, σ_b, according to

$$\sigma_w W = \sigma_b W \lambda \quad (1)$$

where W is the matrix of eigenvectors and λ is the corresponding eigenvalue. W is then sorted according to descending eigenvalues (W_{sort}) and used to project the PC scores into the LD space

$$Y = S_{\{1,2,4,5\}} W_{sort} \quad (2)$$

where $S_{\{1,2,4,5\}}$ is the PCA score matrix containing only PC1, PC2, PC4, and PC5, and Y is the reduced PC score matrix in the LD basis. Finally, the LDA model is tested for accuracy using k-fold cross-validation with k = 10.

RESULTS AND DISCUSSION

Average Raman Spectra and Peak Assignments

Figure 1 shows the average spectra for each of the cell types. Identifiable peak positions are labeled and the accompanying

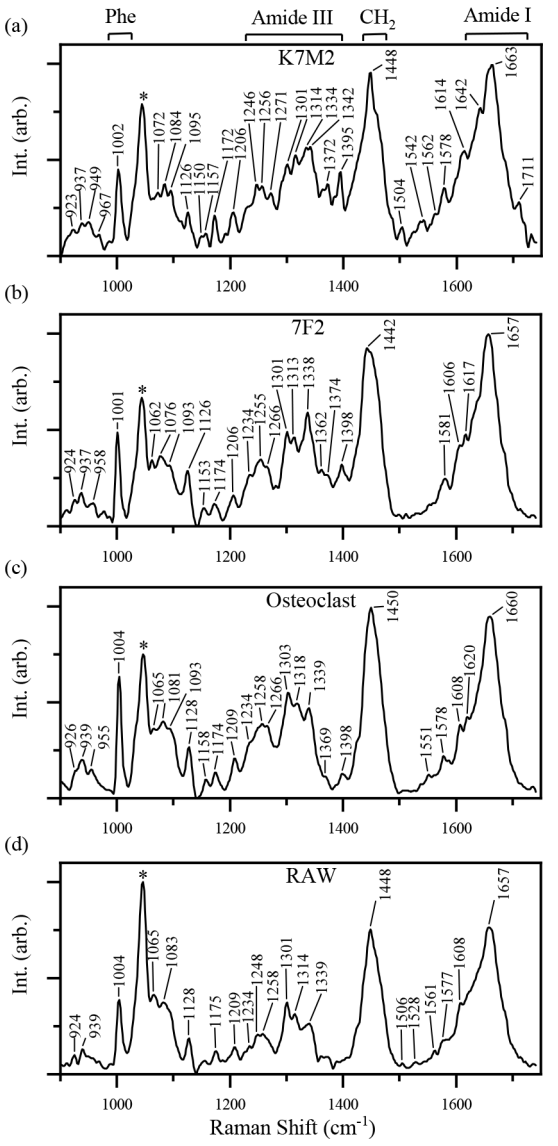

Figure 1. Average Raman spectra of each cell type. (a) K7M2, (b) 7F2, (c) Osteoclast, and (d) RAW. The * indicates the peak associated with the HEPES-based imaging medium.

https://doi.org/10.1021/cbmi.3c00106
Chem. Biomed. Imaging 2024, 2, 147−155

Table 1. Raman Peak Assignments for Each Cell Type[a]

K7M2	7F2	osteoclast	RAW	assignment
923	924	926	924	O−P−O backbone, C−C stretch proline
937	937	939	939	C−C residue α-helix, skeletal modes in polysaccharides
949	958	955		O−P−O symmetric stretch in adenosine-monophosphate, CH_3 deformation (lipid, protein)
967				C−C and C−N stretch PO_3^{2-} stretching DNA
1002	1001	1004	1004	phenylalanine
1072	1062	1065	1065	O−P−O DNA, C−O stretch DNA RNA
1084	1076	1081	1083	O−P−O DNA, C−O stretch DNA RNA
1095	1093	1093		PO_2^- symmetric stretch DNA RNA
1126	1126	1128	1128	Cytochrome C, C−C asymmetric stretch in fatty acids
1157	1153	1158		C−C and C−N stretch in proteins
1172	1174	1174	1175	G-ring stretch, C−C−H bending in phenol ring DNA
1206	1206	1209	1209	C−C stretch, C−H bending, C−C stretch in phenol ring of tyrosine
	1234	1234	1234	antisymmetric phosphate stretching
1246			1248	NH_2 bending in amide III β-sheet
1256	1255	1258	1258	cytosine, adenine
	1266	1266		amide III α-helix
1301	1301	1303	1301	lipids CH_2 twist, protein amide III band, adenine, cytosine
1314	1313	1318	1314	C−H deformation (saturated lipids)
1342	1338	1339	1339	adenine, phenylalanine, C−H deformation, DNA purine bases (CH_3CH_2 wagging mode of polynucleotide chain)
1372	1374	1369		CH_3 symmetric stretching
1395	1398	1398		CH_3 bending due to methyl bond in the membrane
1448	1442	1450	1448	CH_2 stretch deformation of methylene group lipids, CH_2 scissoring in lipids
1504			1506	C=C stretch (aromatics)
1542	1551			amide II N−H bending coupled to C−N stretch
1562			1561	phenylalanine, tryptophan (phenyl, aromatics)
	1606	1608	1608	tyrosine (aromatics)
1642				amide I (protein), C=O stretching of amide coupled to NH_2 in-plane bending
	1657		1657	C=C stretch (lipids), amide I (α-helix, protein)
1663		1660		C=O stretching of amide coupled to NH_2 in-plane bending, amide I (β-sheet, protein)

[a]Peak positions are given in wavenumbers (cm^{-1}). Data from refs 28−42.

assignments are given in Table 1.[28−42] In cases where there is a peak label but no assignment is given, an unambiguous assignment from the existing literature could not be made. In these cases, we refrain from attempting to make an assignment. The primary features of the spectra resemble those typical of osteoblasts and general living cell Raman spectra. Specifically, primary marker peaks of phenylalanine (≈1004 cm^{-1}), amide III (1240−1400 cm^{-1}), CH_2 deformation (1440−1450 cm^{-1}), and amide I (≈1660 cm^{-1}) are observed. One notable difference between the cells is the occurrence of α-helix features in osteoclasts and 7F2 osteoblast cell lines (1657 and 1266 cm^{-1}), which are absent in K7M2 osteosarcoma and RAW cell lines. Rather, K7M2 osteosarcoma and RAW macrophage cell lines exhibit β-sheet features (1246 and 1663 cm^{-1} and 1248 and 1660 cm^{-1}, respectively) which are absent in 7F2 osteoblasts and osteoclasts. An alternative assignment to the ≈1660 cm^{-1} feature is lipid C=C stretch. Thus, the signal from the lipid body likely overlaps the amide I signal and should be considered when evaluating differences between cell types. However, the distinct 1266 and 1246 cm^{-1} peaks strongly suggest that differences in protein structure are observed. Since the shift in the amide I peak is also consistent with a change in protein secondary structure,[30,35] we center our discussion on this interpretation of the results. Overall, from the average spectra, we are beginning to see differences that can serve as markers for cellular classification. Due to the complex nature of the spectra, however, we turn to PCA-LDA to extract the full spectrum of distinguishing features of these cells, which elude the human eye, and use these features for classification.

PCA-LDA Cell Classification

PCA was performed on the combined data set of Raman images from K7M2, 7F2, osteoclast, and RAW cell lines. While separation of classes along principal component axes is a general possibility, we find that there is little to no class separation between these cell types. This is likely because PCA is unsupervised and sets out to capture directions of only maximized variance. LDA, on the other hand, is supervised and captures the directions along class boundaries. Thus, rather than using PCA for classification, we utilize the first five principal components, which account for 74% of the variance (see Figure S1), to reduce the dimensionality of the problem space and remove background spectral and noise contributions. Among the first five principal components, PC3 was found to align primarily with the known spectrum of the HEPES-based imaging medium (Figure S2). Thus, only PC1, PC2, PC4, and PC5 were used to build the linear discriminant model. This removes the need to subtract the background and eliminates artificial class separation by slight differences in the background between cell imaging scans.

The linear discriminant model is built on the PCA scores of PC1, PC2, PC4, and PC5 along with the known class assignments for each pixel. The resulting LD model is then validated in a k-fold cross-validation scheme with $k = 10$. The result of the cross-validation is expressed in Figure 2 as a confusion matrix. Figure 2 shows excellent class prediction accuracy across each of the cell types. 7F2 has a >99% success

https://doi.org/10.1021/cbmi.3c00106
Chem. Biomed. Imaging 2024, 2, 147−155

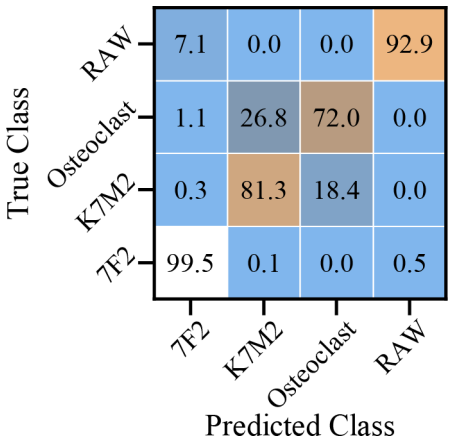

Figure 2. Confusion chart. Shows the predicted class versus the true class for each cell type. Given in percentage of total pixels for each cell type.

rate, while on the lower end, osteoclasts are predicted correctly at a rate of 72%. Interestingly, the K7M2 osteosarcoma line and the induced osteoclasts are the cell types most often erroneously classed as one another. Practically, osteoclasts are much larger in size than osteoblasts making their accurate identification somewhat trivial and independent of their spectral response. Importantly, however, the two morphologically similar 7F2 osteoblast and K7M2 osteosarcoma cell lines are distinguished with a high success rate. The origin of this distinction can be explored by evaluating the LD coefficients and the PCA scores projected onto the LD space.

Figure 3a shows the score distribution projected along linear discriminant axes LD1, LD3, and LD4, according to eq 2. Similar results were obtained replacing LD3 and/or LD4 with LD2. The primary separation occurs along LD1. Figure 3b shows the four LD coefficients. Each of the LD coefficients resembles the original spectra, showing contributions from the four primary marker peaks of phenylalanine, amide III, CH_2 deformation, and amide I. However, intensity contributions vary. While direct interpretation of each of the LD coefficients is difficult, the separation between groups along these axes is apparent, with good separation shown between 7F2, RAW, and osteoclast/K7M2 cell types. The greatest degree of overlap is observed between induced osteoclasts and K7M2 osteosarcoma cells, which reflects the results of the cross-validation where these two cell types were misclassified as each other at the highest rate.

The cell types have been shown to separate well according to the LD model. To evaluate the spectral differences between each cell and identify their differentiating characteristics, we reconstruct the spectra using the LD scores, Y, and PC coefficients, according to

$$R = |YC^{T}_{\{1,2,4,5\}}|^2 \tag{3}$$

where $C_{\{1,2,4,5\}}$ is the matrix of PC loadings for PC1, PC2, PC4, and PC5. The reconstructed spectra for each cell type are shown in Figure 4a, with the color channels used to generate the images indicated. The red channel was chosen to represent amide III and DNA, the green channel was chosen to represent the CH_2 deformation, and the blue channel was chosen to represent amide I. These channel positions are somewhat arbitrary but were chosen to maximize the contrast of features within the cells. Reconstructions are mapped onto cell images in Figure 4b−e. In Figure 4b−e, nuclei are labeled with a white "N" and are characterized by a magenta color in all the cell types due to the predominance of both amide I and amide III signatures as well as strong contributions from nucleic acids that occur in the 1338 cm^{-1} peak overlapping amide III. Two cells in the process of mitosis are indicated with yellow arrows and are characterized by their elongated nuclei (likely metaphase or anaphase, Figure 4e) and attachment (telophase, Figure 4c). Regions outside the cell in Figure 4c,e are characterized by a moderately intense red color and are indicated with an "E". This phenomenon is believed to be a result of the cell secretions or growth media as both 7F2 osteoblasts and RAW 264.7 macrophages are known to secrete components into the media and have high levels of extracellular matrix. In general, the cell cytoplasm appears blue-green in these images due to the prevalence of lipid-rich organelles, which have a signal in the 1300−1450 cm^{-1} region. Lastly, lipids are key components of cellular membranes as well

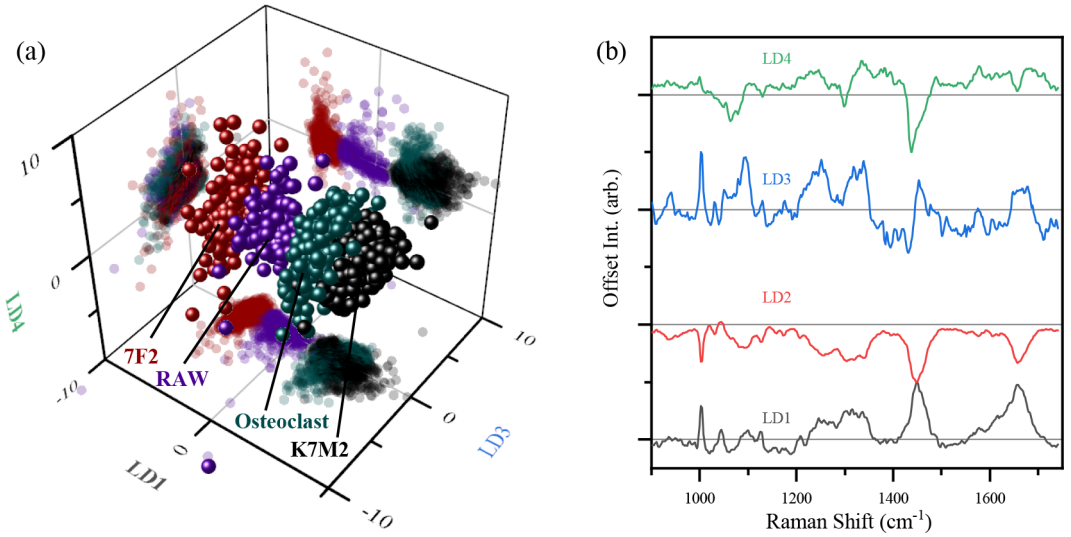

Figure 3. LDA scores and loadings. (a) The PC scores projected onto the LD space along LD1, LD3, and LD4. (b) LD loadings for the four LDs. Loadings are offset for clarity with a solid black y-line indicating the zero-line for each spectrum.

https://doi.org/10.1021/cbmi.3c00106
Chem. Biomed. Imaging 2024, 2, 147−155

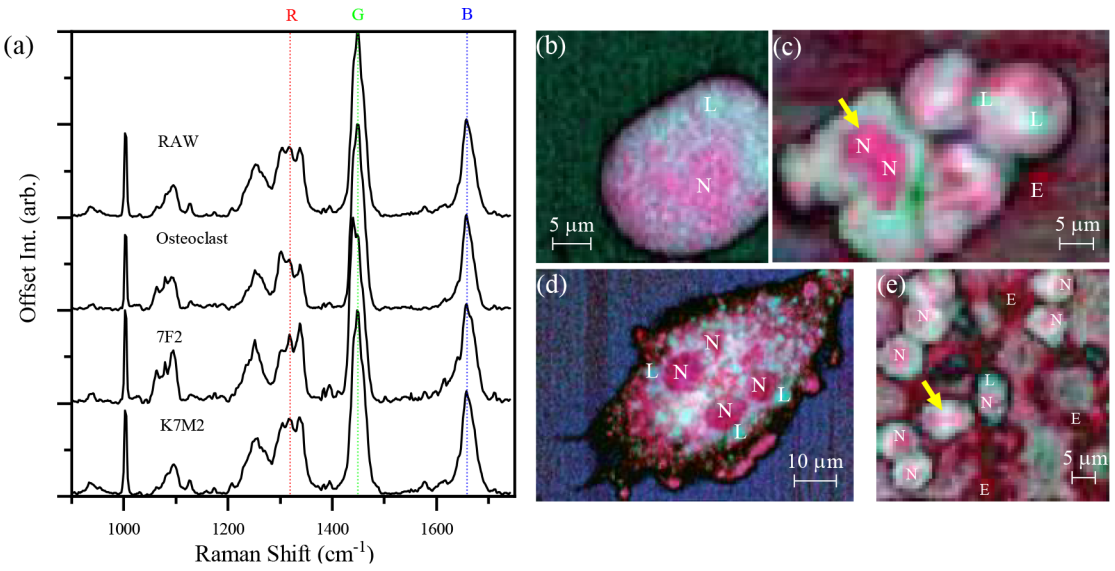

Figure 4. Reconstruction of spectra and images (a) shows the reconstructed spectra, vertically offset for clarity. The vertical lines labeled R, G, and B indicate Raman peaks selected to pseudocolor the image maps in (b)−(e). The red corresponds to the 1338 cm^{-1} vibration and represents DNA and amide III. Green corresponds to the 1445 cm^{-1} vibration and represents CH_2 deformation in lipids, and blue corresponds to the 1657 cm^{-1} vibration and represents amide I. (b−e) Image reconstructions using the LDs for (b) K7M2 osteosarcoma cells, (c) 7F2 osteoblast cells, (d) osteoclast cells, and (e) RAW 264.7 macrophages. Key cellular features in the images are indicated: N = nucleus, L = lipid rich body, and E = extracellular region. Yellow arrows indicate cells in mitosis.

as many cellular organelles including trafficking vesicles, endosomes, and lysosomes. A few, but not all, of the lipid rich bodies are highlighted with a white "L".

The PCA-LDA reconstructions of the spectra highlight the strongest characteristic features of each cell type. We have shown via cross-validation that the discriminant model that comprises these reconstructions accurately classifies each cell type. The reconstructions faithfully reproduce the expected spectral features, determined by a comparison to the original average spectra. To determine why cell lines can be distinguished, we compare their LD reconstructed spectra. The RAW macrophage cell line and the osteoclasts induced from them are distinguished by their spectral reconstruction in several regions. First, the phosphate backbone region takes on a different intensity distribution between the two cell lines. Additionally, a notably higher intensity in the cytochrome C band at 1126 cm^{-1} is observed in the RAW macrophages, compared to the induced osteoclasts. While there does appear to be distinguishing spectral features between these two cell types, classification is trivial due to their size difference. The RAW macrophage cell line has cells with a diameter of ≈10 μm while the induced osteoclast cell line has cells up to 5 times larger. While classification of each cell type is an important goal of this work, our primary objective is to determine whether two cell lines that are visually indistinguishable can be classified. We have shown that PCA-LDA cross-validation could separate 7F2 osteoblasts from K7M2 osteosarcomas. To establish what biochemical differences exist between these two cell types that allow accurate classification, we consider the differences between their reconstructed spectra. Figure 5 shows the resulting difference spectrum between these two cells. The difference was scaled to drive the phenylalanine peak intensity to zero.

The difference spectrum in Figure 5 shows several notable features that can be assigned to physical traits within each cell. Starting from a high wavenumber and working to a low

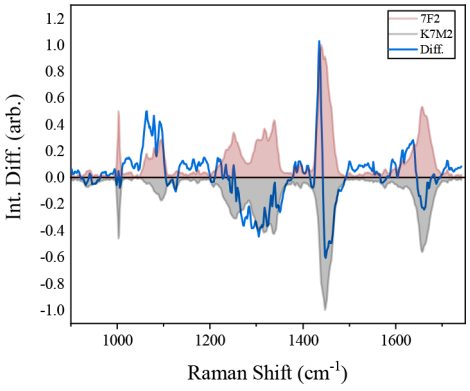

Figure 5. Difference spectra: 7F2 vs K7M2. Shows the reconstructed spectra for 7F2 osteoblast cell line (red) and K7M2 osteosarcoma cell line (gray) as well as the difference spectrum, 7F2 − K7M2, in blue.

wavenumber, we first consider the amide I peak. In this region, the difference spectrum shows a differential feature, suggesting a peak shift between the 7F2 osteoblast cell line and the K7M2 osteosarcoma cell line. Specifically, the K7M2 cell type appears to be upshifted with respect to the 7F2 osteoblast cell line. An upshift in the amide I peak position indicates a difference in protein secondary structure. Higher peak positions of amide I, around 1660−1670 cm^{-1}, are assigned to β-sheet secondary structures. Lower peak positions of amide I, around 1650−1660 cm^{-1}, align with α-helix secondary structures.[30,35] Thus, the difference in amide I peak positions suggests that the K7M2 osteosarcoma cell line may have dominating protein secondary structures of β-sheets while the 7F2 osteoblast cell line dominates in α-helices. This difference was also reflected in the simple average spectra (Figure 1).

The CH_2 deformation peak shows a similar differential character in the difference spectrum, namely, that the peak position for the K7M2 cell type is upshifted from the 7F2 cell type by about 6 cm^{-1}. This is also reflected in the average

https://doi.org/10.1021/cbmi.3c00106
Chem. Biomed. Imaging 2024, 2, 147−155

spectra, albeit with much more noise. Since the CH_2 deformation primarily captures scissoring and stretch deformations in the methylene groups of lipids, the shift in peak position between the K7M2 osteosarcoma and the 7F2 osteoblast cell types highlights that there are likely differences in composition of the lipid membranes between these two cell types. Since lipids play a role in signaling at the membrane, small differences in lipid composition can affect larger differences in function.[43] Recently, altered lipid metabolism in cancer has been identified as an important metabolic change in cancer and associated with cancer progression.[44,45] A difference in the lipid composition between these two cell types is captured by the spectra and may reflect an altered lipid metabolism between the metastatic osteosarcoma cell line, K7M2, and the normal osteoblast cell line, 7F2.

The amide III region shows an overall decrease in intensity in 7F2 cells with respect to that of K7M2 cells. The absolute intensities within this region, however, are difficult to pinpoint. The overall negative feature in the amide III region of the difference spectrum likely captures multiple shifts and intensity differences between the two cells. We can turn to analysis of the average spectra to assist in interpreting the differences in this region. The most notable difference in the average spectra in this region are the features at 1266 cm^{-1} for 7F2 cells and 1246 cm^{-1} for K7M2 cells. These regions are assigned to the amide III α-helix and amide III β-sheet, respectively. This does appear to show through as a possible differential feature in the difference spectrum in Figure 5; however, the multitude of intensity changes make it difficult to discern. However, considering that the amide I feature supports this interpretation and that the average spectra show a clear difference in this region, we assign the primary change in amide III to be associated with a difference in protein secondary structure.

The final region to consider in the difference spectrum is that between 1050 and 1100 cm^{-1}. This region is mostly associated with the phosphate backbone of DNA. While we do observe an increase in the intensity of 7F2 cells versus K7M2 cells, it is not clear how this should be interpreted, with respect to differences between the cells. As the difference between the spectra was scaled to minimize the phenylaline peak, this may be an intensity artifact.

Implications for Differences in Cell Function and Detection

Recently, altered lipid metabolism has been identified as a common phenomenon in cancer cells. These alterations in metabolism can result in increased lipid synthesis, storage, and uptake leading to increased biogenesis for cell membrane production, alterations in cell signaling, and energy production.[44] Alterations in lipid metabolism are also associated with oncogenic signaling and crosstalk with the tumor microenvironment resulting in increased tumor cell survival in the tumor microenvironment, therapeutic resistance, and metastatic potential.[44,45] In osteosarcoma, altered lipid composition has been noted between metastatic and nonmetastatic human osteosarcoma cell lines and normal osteoblasts.[46] Lipid composition and lipid metabolism have not previously been studied in mouse osteosarcoma models; however, the research presented here demonstrates differences in lipid composition in mouse osteosarcoma versus osteoblast cell lines as well. Alterations in lipid metabolism are also known to occur in osteosarcoma patients, and recent work has shown that specific alterations may also have prognostic implications.[47,48] While the metabolic changes in lipid metabolism have not been studied in the K7M2 osteosarcoma cell line, the observed differences in lipid composition suggest that there are likely changes in lipid metabolism. As changes in lipid metabolism are being considered targets for therapeutic intervention, further studies of the exact alterations in lipid metabolism and lipid composition present in the K7M2 osteosarcoma model system could further validate this model for testing therapeutic development.

Also observed was a shift in the K7M2 osteosarcoma cell line toward the β-sheet secondary protein structure versus the α-helix secondary structure present in the 7F2 osteoblast cell line. To our knowledge, this is the first time this alteration has been found in a comparison of osteosarcoma and osteoblasts. However, previous studies have demonstrated increased β-sheet content compared to α-helix in extracellular vesicles derived from patients with prostate cancer, pancreatic cancer cell lines, and associated extracellular vesicles and extracellular vesicles derived from pancreatic cancer patients.[49,50] Measurements of this richness in β-sheet secondary structure combined with spectral signatures of DNA methylation using hyperspectral confocal Raman microscopy have also been utilized to differentiate different types of prostate cancer.[51] While most of these types of studies are focused on diagnostics, the ability to differentiate cell type demonstrated in these studies as well as the current study highlights the potential to follow cellular interactions between cancer cells and normal cells within the tumor environment, label-free, in multicellular models.

CONCLUSION

We have shown that cell types in a multicellular model can be distinguished and classified using noninvasive, label-free hyperspectral confocal Raman microscopy. This was done by building a library of reference cell spectra from images of normal occurring bone cell types, 7F2 osteoblast cell line, induced osteoclasts, and osteoclast precursor, macrophage cell line RAW 264.7, and the K7M2 osteosarcoma bone cancer cell line. These spectra were used to build a linear discriminant model using a combination of PCA and LDA. The PCA-LDA model was tested using cross-validation, which showed good prediction accuracy. Spectra were reconstructed from the PCA-LDA model and analyzed. Specifically, spectral features of 7F2 osteoblast and K7M2 osteosarcoma cell lines were compared to determine the confounding physical features distinguishing osteoblasts from osteosarcomas. We found that the osteosarcoma cancer cell line, K7M2, had a dominant signal originating from the β-sheet protein secondary structure while the normal osteoblast cell line 7F2 showed primarily α-helix secondary structure. Additionally, the lipid composition between the K7M2 osteosarcoma cell line and the 7F2 osteoblast cell line was differentiated by the CH_2 deformation peak, which indicates potential differences in signaling and, thus, overall function. While the details of how these differences manifest in differences in cell function between osteosarcoma and osteoblast cell types remain to be explored, the observations are consistent with the recent growing literature highlighting alterations in protein structure and lipid composition as indicative of cancer cell malignancy. We showed that hyperspectral confocal Raman microscopy can serve as an effective tool for extracting feature differences between these cell types and, importantly, for distinguishing them in *in vitro* models and *in vivo* in a nondestructive, label-free manner.

https://doi.org/10.1021/cbmi.3c00106
Chem. Biomed. Imaging 2024, 2, 147−155

■ ASSOCIATED CONTENT

Data Availability Statement

All data and code used to generate results are available from the authors by request.

Supporting Information

The Supporting Information is available free of charge at https://pubs.acs.org/doi/10.1021/cbmi.3c00106.

Additional figures showing the total variance explained by PCA and plots of the PC loadings (PDF)

■ AUTHOR INFORMATION

Corresponding Authors

Zachary T. Piontkowski − *Sandia National Laboratories, Department of Applied Optics and Plasma Sciences, Albuquerque, New Mexico 87123, United States;* orcid.org/0000-0002-6282-0106; Email: ztpiont@sandia.gov

Jerilyn A. Timlin − *Sandia National Laboratories, Department of Molecular and Microbiology, Albuquerque, New Mexico 87123, United States*; Email: jatimli@sandia.gov

Authors

Dulce C. Hayes − *Sandia National Laboratories, Department of Molecular and Microbiology, Albuquerque, New Mexico 87123, United States*

Anthony McDonald − *Sandia National Laboratories, Department of Applied Optics and Plasma Sciences, Albuquerque, New Mexico 87123, United States*

Kalista Pattison − *Sandia National Laboratories, Department of Molecular and Microbiology, Albuquerque, New Mexico 87123, United States*

Kimberly S. Butler − *Sandia National Laboratories, Department of Molecular and Microbiology, Albuquerque, New Mexico 87123, United States;* orcid.org/0000-0001-6045-8636

Complete contact information is available at: https://pubs.acs.org/10.1021/cbmi.3c00106

Notes

The authors declare no competing financial interest.

■ ACKNOWLEDGMENTS

This work was performed under the Laboratory Directed Research and Development (LDRD) program at Sandia National Laboratories. Sandia National Laboratories is a multimission laboratory managed and operated by National Technology and Engineering Solutions of Sandia, LLC, a wholly owned subsidiary of Honeywell International, Inc., for the U.S. Department of Energy's National Nuclear Security Administration under contract DE-NA-0003523. The views expressed in this article do not necessarily represent the views of the U.S. DOE or the United States Government.

■ REFERENCES

(1) Kasprowicz, R.; Suman, R.; O'Toole, P. *Int. J. Biochem. Cell Biol.* **2017**, *84*, 89−95.

(2) Jeon, S.; Kim, J.; Lee, D.; Baik, J. W.; Kim, C. *Photoacoustics* **2019**, *15*, 100141.

(3) Georgakoudi, I.; Quinn, K. P. *Annu. Rev. Biomed Eng.* **2023**, *25*, 413−443.

(4) Yue, J.; Liu, Z.; Cai, X.; Ding, X.; Chen, S.; Tao, K.; Zhao, T. *Talanta* **2016**, *150*, 503−9.

(5) Kumamoto, Y.; Harada, Y.; Takamatsu, T.; Tanaka, H. *Acta Histochem Cytochem* **2018**, *51*, 101−110.

(6) El-Mashtoly, S. F.; Gerwert, K. *Anal. Chem.* **2022**, *94*, 120−142.

(7) Mandair, G. S.; Morris, M. D. *Bonekey Rep* **2015**, *4*, 620.

(8) Morris, M. D.; Mandair, G. S. *Clin Orthop Relat Res.* **2011**, *469*, 2160−9.

(9) Ishimaru, Y.; Oshima, Y.; Imai, Y.; Iimura, T.; Takanezawa, S.; Hino, K.; Miura, H. *Molecules* **2018**, *23*, 3081.

(10) Khan, A. F.; Awais, M.; Khan, A. S.; Tabassum, S.; Chaudhry, A. A.; Rehman, I. U. *Appl. Spectrosc. Rev.* **2013**, *48*, 329−355.

(11) Krafft, C.; Schmitt, M.; Schie, I. W.; Cialla-May, D.; Matthäus, C.; Bocklitz, T.; Popp, J. *Angew. Chem., Int. Ed. Engl.* **2017**, *56*, 4392−4430.

(12) Lau, C. P. Y.; Ma, W.; Law, K. Y.; Lacambra, M. D.; Wong, K. C.; Lee, C. W.; Lee, O. K.; Dou, Q.; Kumta, S. M. *Analyst* **2022**, *147*, 1425−1439.

(13) D'Acunto, M.; Trombi, L.; D'Alessandro, D.; Danti, S. *Phys. Biol.* **2019**, *16*, 016007.

(14) Siddiqui, J. A.; Partridge, N. C. *Physiology (Bethesda)* **2016**, *31*, 233−45.

(15) Kim, J.-M.; Lin, C.; Stavre, Z.; Greenblatt, M. B.; Shim, J.-H. *Cells* **2020**, *9*, 2073.

(16) Misaghi, A.; Goldin, A.; Awad, M.; Kulidjian, A. A. *Sicot j* **2018**, *4*, 12.

(17) Thrivikraman, G.; Athirasala, A.; Gordon, R.; Zhang, L.; Bergan, R.; Keene, D. R.; Jones, J. M.; Xie, H.; Chen, Z.; Tao, J.; Wingender, B.; Gower, L.; Ferracane, J. L.; Bertassoni, L. E. *Nat. Commun.* **2019**, *10*, 3520.

(18) Clarke, M. S.; Sundaresan, A.; Vanderburg, C. R.; Banigan, M. G.; Pellis, N. R. *Acta Biomater* **2013**, *9*, 7908−16.

(19) Bernhardt, A.; Skottke, J.; Von Witzleben, M.; Gelinsky, M. *International Journal of Molecular Sciences* **2021**, *22*, 7316.

(20) Li, J.; Li, J.; Wang, H.; Qin, J.; Zeng, H.; Wang, K.; Wang, S. *Biomed Opt Express* **2021**, *12*, 5514−5528.

(21) Hashimoto, A.; Yamaguchi, Y.; Chiu, L.-D.; Morimoto, C.; Fujita, K.; Takedachi, M.; Kawata, S.; Murakami, S.; Tamiya, E. *Sci. Rep.* **2015**, *5*, 12529.

(22) Cao, Y.; Zhou, Z.; de Crombrugghe, B.; Nakashima, K.; Guan, H.; Duan, X.; Jia, S. F.; Kleinerman, E. S. *Cancer Res.* **2005**, *65*, 1124−8.

(23) Bertin, H.; Guilho, R.; Brion, R.; Amiaud, J.; Battaglia, S.; Moreau, A.; Brouchet-Gomez, A.; Longis, J.; Piot, B.; Heymann, D.; Corre, P.; Rédini, F. *J. Transl Med.* **2019**, *17*, 56.

(24) Grisez, B. T.; Ray, J. J.; Bostian, P. A.; Markel, J. E.; Lindsey, B. A. *J. Orthop Res.* **2018**, *36*, 2296.

(25) Brown, P. S.; Wang, E.; Aroeti, B.; Chapin, S. J.; Mostov, K. E.; Dunn, K. W. *Traffic* **2000**, *1*, 124−40.

(26) Collin-Osdoby, P.; Osdoby, P. *Methods Mol. Biol.* **2012**, *816*, 187−202.

(27) Xiao, Y.; Karttunen, M.; Jalkanen, J.; Mussi, M. C.; Liao, Y.; Grohe, B.; Lagugné-Labarthet, F.; Siqueira, W. L. *J. Dent Res.* **2015**, *94*, 1106−12.

(28) Ma, C.; Zhang, L.; He, T.; Cao, H.; Ren, X.; Ma, C.; Yang, J.; Huang, R.; Pan, G. *Stem Cell Research & amp; Therapy* **2021**, *12*, 555.

(29) Tang, W.; Newton, R. J.; Xie, C. A.; Li, Y. Q.; Whitley, N. *Genomics Proteomics Bioinformatics* **2005**, *3*, 169−78.

(30) Aksoy, C.; Severcan, F. *Spectroscopy: An International Journal* **2012**, *27*, 167−184.

(31) Sharma, A.; Goring, A.; Staines, K. A.; Emery, R. J. H.; Pitsillides, A. A.; Oreffo, R. O. C.; Mahajan, S.; Clarkin, C. E. *Matrix Biol. Plus* **2020**, *5*, 100018.

(32) McManus, L. L.; Bonnier, F.; Burke, G. A.; Meenan, B. J.; Boyd, A. R.; Byrne, H. J. *Analyst* **2012**, *137*, 1559.

(33) Hashimoto, A.; Yamaguchi, Y.; Chiu, L.-D.; Morimoto, C.; Fujita, K.; Takedachi, M.; Kawata, S.; Murakami, S.; Tamiya, E. *Sci. Rep.* **2015**, *5*, 12529.

(34) Chiang, Y. H.; Wu, S. H.; Kuo, Y. C.; Chen, H. F.; Chiou, A.; Lee, O. K. *Stem Cell Res. Ther* **2015**, *6*, 81.
(35) Kukolj, T.; Lazarević, J.; Borojević, A.; Ralević, U.; Vujić, D.; Jauković, A.; Lazarević, N.; Bugarski, D. *International Journal of Molecular Sciences* **2022**, *23*, 4915.
(36) Bai, H.; Chen, P.; Fang, H.; Lin, L.; Tang, G. Q.; Mu, G. G.; Gong, W.; Liu, Z. P.; Wu, H.; Zhao, H.; Han, Z. C. *Laser Physics Letters* **2011**, *8*, 78−84.
(37) Notingher, I.; Bisson, I.; Bishop, A. E.; Randle, W. L.; Polak, J. M. P.; Hench, L. L. *Anal. Chem.* **2004**, *76*, 3185−3193.
(38) Wiercigroch, E.; Szafraniec, E.; Czamara, K.; Pacia, M. Z.; Majzner, K.; Kochan, K.; Kaczor, A.; Baranska, M.; Malek, K. *Spectrochim Acta A Mol. Biomol Spectrosc* **2017**, *185*, 317−335.
(39) Clemens, G.; Hands, J. R.; Dorling, K. M.; Baker, M. J. *Analyst* **2014**, *139*, 4411−4444.
(40) Czamara, K.; Majzner, K.; Pacia, M. Z.; Kochan, K.; Kaczor, A.; Baranska, M. *J. Raman Spectrosc.* **2015**, *46*, 4−20.
(41) De Gelder, J.; De Gussem, K.; Vandenabeele, P.; Moens, L. *J. Raman Spectrosc.* **2007**, *38*, 1133−1147.
(42) Pezzotti, G.; Zhu, W.; Adachi, T.; Horiguchi, S.; Marin, E.; Boschetto, F.; Ogitani, E.; Mazda, O. *Journal of Cellular Physiology* **2020**, *235*, 5146−5170.
(43) Horn, A.; Jaiswal, J. K. *Curr. Top Membr.* **2019**, *84*, 67−98.
(44) Fu, Y.; Zou, T.; Shen, X.; Nelson, P. J.; Li, J.; Wu, C.; Yang, J.; Zheng, Y.; Bruns, C.; Zhao, Y.; Qin, L.; Dong, Q. *MedComm* **2021**, *2* (2), 27−59.
(45) Jeong, D.-W.; Lee, S.; Chun, Y.-S. *Lipids in Health and Disease* **2021**, *20*, 163.
(46) Roy, J.; Dibaeinia, P.; Fan, T. M.; Sinha, S.; Das, A. *J. Lipid Res.* **2019**, *60*, 375−387.
(47) Li, Z.; Jin, C.; Lu, X.; Zhang, Y.; Zhang, Y.; Wen, J.; Liu, Y.; Liu, X.; Li, J. *J. Gene Med.* **2023**, *25*, No. e3491.
(48) Qian, H.; Lei, T.; Hu, Y.; Lei, P. *Front Cell Dev Biol.* **2021**, *9*, 673827.
(49) Krafft, C.; Wilhelm, K.; Eremin, A.; Nestel, S.; von Bubnoff, N.; Schultze-Seemann, W.; Popp, J.; Nazarenko, I. *Nanomedicine* **2017**, *13*, 835−841.
(50) Rasuleva, K.; Elamurugan, S.; Bauer, A.; Khan, M.; Wen, Q.; Li, Z.; Steen, P.; Guo, A.; Xia, W.; Mathew, S.; Jansen, R.; Sun, D. *ACS Sens.* **2021**, *6*, 4489−4498.
(51) Szymoński, K.; Lipiec, E.; Sofińska, K.; Skirlińska-Nosek, K.; Czaja, M.; Seweryn, S.; Wilkosz, N.; Birarda, G.; Piccirilli, F.; Vaccari, L.; Chmura, L.; Szpor, J.; Adamek, D.; Szymoński, M. *Eur. J. Nucl. Med. Mol. Imaging* **2023**, *50*, 1792−1810.

https://doi.org/10.1021/cbmi.3c00106
Chem. Biomed. Imaging 2024, 2, 147−155